The impact of filaments on dwarf galaxy properties in the Auriga simulations

Haonan Zheng [1,2]★ Shihong Liao [1,3]★ Jia Hu [1,2] Liang Gao,[1,2,4] Robert J. J. Grand [5,6,7] Qing Gu[1,2] and Qi Guo[1,2]

[1] *Key Laboratory for Computational Astrophysics, National Astronomical Observatories, Chinese Academy of Sciences, Beijing 100012, China*
[2] *University of Chinese Academy of Sciences, 19 A Yuquan Rd, Shijingshan District, Beijing 100049, China*
[3] *Department of Physics, University of Helsinki, Gustaf Hällströmin katu 2, FI-00014 Helsinki, Finland*
[4] *Institute for Computational Cosmology, Department of Physics, University of Durham, South Road, Durham DH1 3LE, UK*
[5] *Max-Planck-Institut für Astrophysik, Karl-Schwarzschild-Str. 1, D-85748 Garching, Germany*
[6] *Instituto de Astrofísica de Canarias, Calle Vía Láctea s/n, E-38205 La Laguna, Tenerife, Spain*
[7] *Departamento de Astrofísica, Universidad de La Laguna, Av. del Astrofísico Francisco Sánchez s/n, E-38206 La Laguna, Tenerife, Spain*

ABSTRACT

With a hydrodynamical simulation using a simple galaxy formation model without taking into account feedback, our previous work has shown that dense and massive filaments at high redshift can provide potential wells to trap and compress gas, and hence affect galaxy formation in their resident low-mass haloes. In this paper, we make use of the Auriga simulations, a suite of high-resolution zoom-in hydrodynamical simulations of Milky Way-like galaxies, to study whether the conclusion still holds in the simulations with a sophisticated galaxy formation model. In agreement with the results of our previous work, we find that, compared to their counterparts with similar halo masses in the field, dwarf galaxies residing in filaments tend to have higher baryonic and stellar fractions. At the fixed parent halo mass, the filament dwarfs tend to have slightly higher star formation rates than those of field ones. But overall we do not find a clear difference in galaxy $g - r$ colours between the filament and field populations. We also show that at high redshifts, the gas components in dwarf galaxies tend to have their spins aligned with the filaments in which they reside. Our results support a picture in which massive filaments at high redshift assist gas accretion and enhance star formation in their resident dwarf-sized dark matter haloes.

Key words: methods: numerical – Galaxy: formation – Galaxy: halo.

1 INTRODUCTION

In the standard galaxy formation framework (e.g. White & Rees 1978; White & Frenk 1991), dark matter haloes provide potential wells to compress gas and then the subsequent physics, e.g. radiative cooling, star formation, stellar and black hole feedback, and so on, proceed to form galaxies. Similarly to dark matter haloes, dense and massive filaments at high redshift can also provide deep potential wells to trap and compress gas and provide sites for galaxy formation.

The impact of filaments on galaxy formation is particularly prominent in warm dark matter (WDM) models: Gao & Theuns (2007) show that the first stars can directly form in the potential wells of massive filaments in WDM models; Gao, Theuns & Springel (2015) further show with hydrodynamical simulations that smooth and dense filaments rather than haloes dominate star formation at $z \gtrsim 6$ in WDM models. In the cold dark matter (CDM) paradigm, as shown by Kereš et al. (2005) and many other follow-up works, CDM filaments can direct gas flows to the centres of massive galaxies (see also e.g. Dekel & Birnboim 2006; Ocvirk, Pichon & Teyssier 2008; Brooks et al. 2009; Dekel et al. 2009; Kereš et al. 2009). Recently,

with a hydrodynamical version of the zoom-in Aquarius simulation (Springel et al. 2008), Liao & Gao (2019, hereafter LG19) further show that, apart from feeding massive central galaxies, high-redshift filaments indeed compress gas, and so assist gas cooling and enhance star formation in their resident low-mass dark matter haloes.

In LG19, in order to investigate gas accretion and cooling in filaments and their low-mass dark matter haloes, as a first step, the authors neglected the stellar feedback effects in their simulations. In this work, we use the Auriga simulations (Grand et al. 2017), a series of high-resolution runs with more realistic galaxy formation models (especially including supernovae and black hole feedback processes), to study the impact of filaments on galaxy formation in their resident dwarf dark matter haloes.

This paper is organized as follows. Section 2 describes the details of simulations and our filament identification method. Our results and conclusions are presented in Sections 3 and 4, respectively. Resolution studies are given in Appendix A.

2 THE SIMULATIONS AND FILAMENT IDENTIFICATION

We use the hydrodynamical zoom-in simulations of the Auriga project (Grand et al. 2017), which consist of 30 isolated Milky

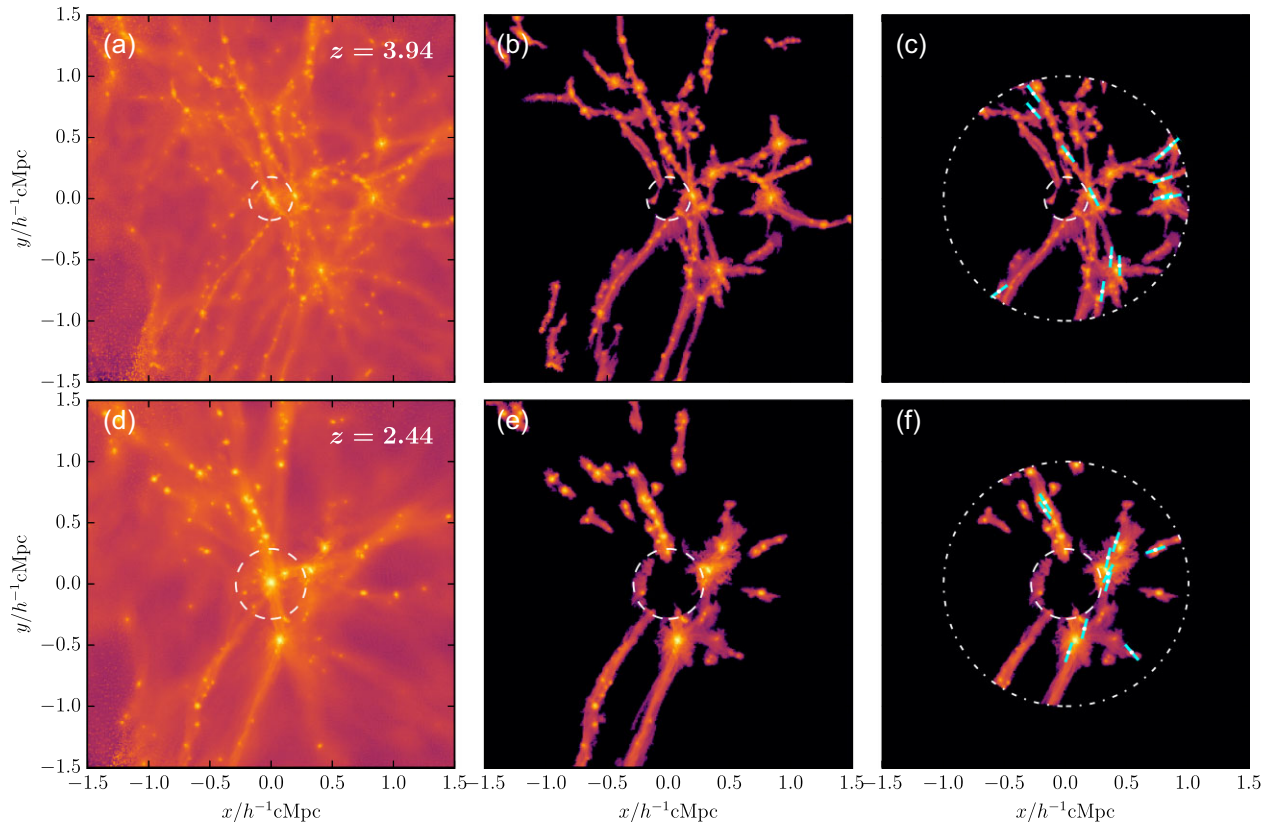★ E-mail: hnzheng@nao.cas.cn (HZ); shliao@nao.cas.cn (SL)

Figure 1. Panel (a): xy-projected CIC baryonic density field of the Au-27 simulation at $z = 3.94$. The white dashed circles in all panels mark the radius $2R_{200, \text{MW}}$ centred on the main halo. Panel (b): filaments identified with the method described in LG19. Panel (c): short cyan lines overplotted on the density field show the projected directions of the filament at random galaxies. The dash–dotted circle shows the radius of $1.0\ h^{-1}$ cMpc within which our galaxy sample is chosen. Panels (d)–(f): similar to panels (a)–(c), but for a redshift of $z = 2.44$.

Way-sized galaxies and their surroundings with the AREPO code (Springel 2010). Each Auriga simulation is labelled as 'Au-*X*' with *X* ranging from 1 to 30. The cosmological parameters correspond to the Planck results: $\Omega_{\text{m}} = 0.307$, $\Omega_{\Lambda} = 0.693$, $\Omega_{\text{b}} = 0.048$, and $h = 0.6777$ (Planck Collaboration et al. 2014). For the Level 4 resolution simulations that we use in this analysis, the initial masses of baryon and high-resolution dark matter particles are $m_{\text{b}} \sim 5 \times 10^4\ \text{M}_{\odot}$ and $m_{\text{DM}} \sim 3 \times 10^5\ \text{M}_{\odot}$, respectively. The gravitational softening length, ϵ, for star and high-resolution dark matter particles is set as $500\ h^{-1}$ cpc before $z = 1$, and fixed at 369 pc later. As for gas cells, the softening length is adjusted according to their mean radius, from $500\ h^{-1}$ cpc (369 pc after $z = 1$) to 1.85 kpc. Haloes and subhaloes are identified with the friends-of-friends (FOF; Davis et al. 1985) and SUBFIND algorithm (Springel et al. 2001), respectively. We refer the reader to Grand et al. (2017) for a detailed description of the Auriga simulations.

To identify filaments in each Auriga simulation, we use the method proposed in LG19, which is based on the baryonic density field and the Hoshen–Kopelman algorithm (Hoshen & Kopelman 1976). In this method, we consider all baryonic particles/cells (i.e. gas and stars) in the zoom-in simulation region. Note that the zoom-in region in different Auriga runs has different shapes and spatial extents, and we have chosen a fixed $3\ h^{-1}$ cMpc cubic region centring the Milky Way-like galaxy centre[1] for all 30 Auriga runs. Then, we

compute the baryonic density field of this cubic region on 512^3 grid cells using the cloud-in-cell (CIC) method. See panels (a) and (d) of Fig. 1 for examples of the projected baryonic density fields at two redshifts from the Au-27 simulation. We further exclude the central region within twice the virial radius of the main halo (the dashed circles in Fig. 1) as well as the cells whose overdensity is lower than a given threshold Δ_{th}, link neighbouring cells as structures using the Hoshen–Kopelman algorithm, and define those structures with sizes (i.e. the number of containing grid cells) larger than a given size threshold S_{th} as 'filaments'. The rest of the region outside the excluded central sphere is defined as 'field'. Like the overdensity parameter in spherical overdensity halo finder, Δ_{th} is a free parameter to control the overdensity and boundary of a filament, and S_{th} is used to exclude small isolated high-density regions (which are usually related to isolated large galaxies) from filament classification. These two free parameters regulate how prominent the detected filaments are, with higher values for them, the detected filaments will be more overdense and have larger sizes. In this work, the two threshold parameters are set to $\Delta_{\text{th}} = 3.0$ and $S_{\text{th}} = 3000$, which return good filament structures according to human eyes' judgements; see panels (b) and (e) of Fig. 1 for examples. Following LG19, we also only consider high-redshift dense filaments at $z \sim 4$ and ~ 2.5 in this study, as low-redshift filaments have less impact on galaxy formation (Gao et al. 2015). Note that we have varied the values of Δ_{th} and S_{th} and confirmed that the results presented in the following sections are not sensitive to the choices of these parameter values. For example, we have tried with $(\Delta_{\text{th}}, S_{\text{th}}) = (2.0, 3000)$, $(4.0, 3000)$, $(3.0, 2000)$, $(3.0, 4000)$, and $(3.5, 1000)$, the quantitative difference of the

[1]The centre of a galaxy is defined as the position of the particle with the minimum gravitational potential energy in the FOF group.

baryonic fraction–virial mass relations (which will be discussed in the next section) is just a few per cent.

We have also varied the number of grid cells when computing the CIC density field in the $3\,h^{-1}$ cMpc cubic region, and made sure that our results do not sensitively depend on the number of grid cells. For example, we have tested with 256^3 grid cells, and with $\Delta_{th} = 3.0$ and $S_{th} = 375$, the baryonic fraction–virial mass relation only differs from our fiducial results at a level of a few per cent.

In this study, a galaxy consists of all types of particles/cells within the virial radius,[2] R_{200}, of the corresponding FOF group. If the centre of a galaxy is located in a classified filament (field) environment, then this galaxy is called a filament (field) galaxy. Note that in order to avoid the influence from the main galaxies and contamination by low-resolution particles from the outer parts of the simulation volume, we only use galaxies whose comoving distance from the main galaxy centre, d, satisfies $2R_{200,\,MW} < d < 1.0\,h^{-1}$ cMpc, where $R_{200,\,MW}$ denotes the comoving virial radius of the main central galaxy. In our parent galaxy sample, we only consider galaxies with virial masses (i.e. the total mass within R_{200}) $M_{200} \geq 10^8\,h^{-1}\,\mathrm{M_\odot}$, which contain at least 350 dark matter particles. In total, at $z = 3.94$ (2.44), we have 4192 (2736) filament galaxies and 11 036 (13 464) field galaxies in our parent sample from all 30 Auriga simulations. Note that the resolution requirement of $\geq$350 dark matter particles for the parent sample is similar to those adopted in previous literature when studying halo baryonic fractions (e.g. Crain et al. 2007; Okamoto, Gao & Theuns 2008) and stellar fractions (e.g. Puchwein & Springel 2013). As detailed in the following sections, we will place additional resolution requirements on the baryonic particle number when computing the star formation rates, galaxy colours, and galaxy spins.

Note that apart from the aforementioned 30 Level 4 resolution runs, the Auriga project has additional 6 Level 3 runs with ~8 times higher resolution (i.e. Au-6, Au-16, Au-21, Au-23, Au-24, and Au-27). We have performed a resolution convergence study with six Auriga simulations from both the Level 3 and Level 4 runs, and confirm that the results presented in the following sections do not suffer from numerical resolution issues (see Appendix A for details). In order to have better statistics, in the following, we mainly show results from the 30 Level 4 runs.

3 RESULTS

3.1 Baryonic fractions and stellar fractions

Using their simulations with a simple galaxy formation model, LG19 have shown that, compared to the dwarf galaxies in the field, the dwarfs in filaments with the same halo mass tend to have higher baryonic fractions and stellar fractions, suggesting that filaments play a significant role in assisting gas cooling and star formation. Since they studied with a simple hydrodynamic version of the Aquarius simulation (Springel et al. 2008), which does not include any feedback mechanism, here we re-examine these results with the Auriga simulations to see how these results vary in hydrodynamical simulations with more realistic galaxy formation models.

Following LG19, we define the baryonic fraction of a galaxy as $f_{bar} \equiv M_{bar}/M_{200}$, where M_{bar} is the baryonic mass (including gas and stellar masses) within the virial radius R_{200}. In Fig. 2, we display baryonic fractions for filament (red dots) and field galaxy (blue dots)

of our galaxy sample at redshift $z = 3.94$ (left-hand panel) and $z = 2.44$ (right-hand panel), respectively, as the median values for filament and field galaxies are shown with red and blue lines, and the scatters (i.e. the 16th and 84th percentiles) in each mass bin are shown with the error bars. In the bottom panels, we plot the ratio between the median baryonic fraction of filament galaxies and that of field ones, and the error of the ratio is computed from error propagation, i.e. $\delta(x_{fila}/x_{field}) = \sqrt{(\delta x_{fila}/x_{field})^2 + (x_{fila}\delta x_{field}/x_{field}^2)^2}$. Note that performing error propagation with asymmetric errors from the upper panels is not a trivial task (see e.g. Barlow 2004; Audi et al. 2017; Possolo, Merkatas & Bodnar 2019). Here, we first follow the 'Method 2' in appendix A of Audi et al. (2017) to estimate the equivalent symmetric errors (i.e. δx_{fila} and δx_{field}) and median values (i.e. x_{fila} and x_{field}) for both filament and field galaxies in each mass bin, and then use the aforementioned error propagation formula to compute the error of the ratio. Note that as there are very few field galaxies with $M_{200} \gtrsim 10^{9.5}\,h^{-1}\,\mathrm{M_\odot}$ in the Auriga simulations, here we only plot and focus on the galaxies with $M_{200} \leq 10^{9.5}\,h^{-1}\,\mathrm{M_\odot}$ in both environments.

During the cosmic reionization, as the ultraviolet background produced by quasars and stars heats the gas via the photoheating process, the gas becomes too hot to be confined by the gravitational potential wells of low-mass dark matter haloes, leading to a decrease in baryonic fractions in lower mass haloes. We observe here that, below $M_{200} \lesssim 10^{9.5}\,h^{-1}\,\mathrm{M_\odot}$, the baryonic fractions of galaxies in both filaments and field decrease with halo masses, in agreement with previous results (e.g. Okamoto et al. 2008). We also note that the characteristic mass, defined as the galaxy virial mass at which the median baryonic fraction is half of the cosmic baryonic fraction (Ω_b/Ω_m), increases with time for both filament and field galaxies, i.e. the characteristic mass is $M_c \sim 10^{8.5}\,h^{-1}\,\mathrm{M_\odot}$ at $z \sim 4$, while it is $M_c \sim 10^9\,h^{-1}\,\mathrm{M_\odot}$ at $z \sim 2.5$. This redshift dependence of characteristic mass is mainly a result of reionization and hierarchical halo assembly (see Okamoto et al. 2008, for a detailed semi-analytical model to explain this). We also expect that the supernova feedback, which is not included in Okamoto et al. (2008), partially contributes to the evolution of characteristic mass as the feedback heats and enriches gas, which consequently affects the heating and cooling processes and the gas equilibrium temperature.

Overall, at fixed halo mass, filament galaxies tend to have a higher baryonic fraction than those in the field, and this enhancement of the baryonic fraction in filament galaxies is larger with decreasing halo mass. At $M_{200} \sim 10^8\,h^{-1}\,\mathrm{M_\odot}$, the median baryonic fraction for filament galaxies is approximately five times that for field ones. The effects are observed at both $z \approx 4$ and $z \approx 2.5$.

Quantitatively, these results are very similar to those in LG19. For example, in LG19, at $z = 4$, as the galaxy mass decreases from ~10^9 to $10^{7.5}\,h^{-1}\,\mathrm{M_\odot}$, the ratio between the median baryonic fractions of filament galaxies and field galaxies increases from ~1.1 to ~5; for galaxies with $M_{200} \sim 10^8\,h^{-1}\,\mathrm{M_\odot}$, this ratio is ~3. This implies that adding supernova feedback has a small effect on the f_{bar} difference between filament and field high-z dwarf galaxies.

We notice that there are a fraction of galaxies that have baryonic fractions higher than the cosmic mean value (i.e. $\Omega_b/\Omega_m \approx 0.16$), especially in the filament environment. One cause is the environmental effects, i.e. as the Auriga simulations focus on overdense zoom-in regions with stronger baryon inflows compared to the cosmic average, the baryonic fractions can be a little bit higher than the cosmic mean value, especially in the high-density filament environment. Another cause is that some haloes are splashback haloes, i.e. they used to be subhaloes in the history and some fraction of the outer dark matter mass was tidally stripped away and left with

---

[2]The virial radius of a galaxy is defined as the radius within which the mean mass density is 200 times the critical density of the universe.
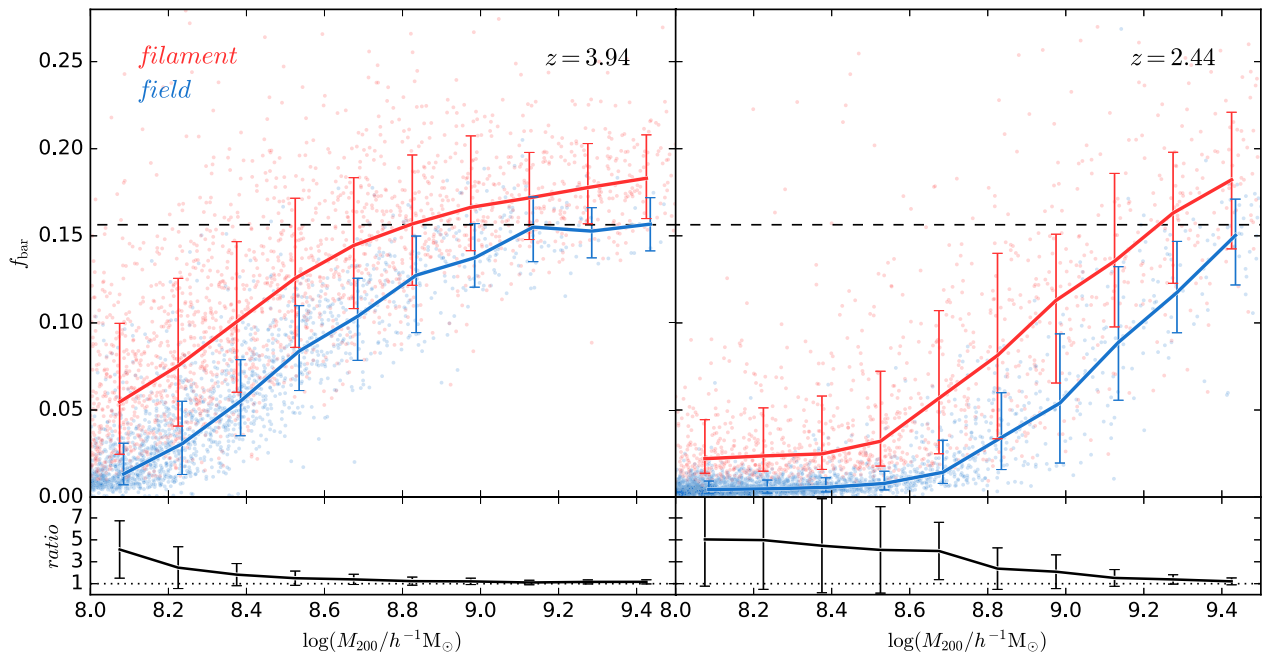
Figure 2. Relation between baryonic fraction, f_{bar}, and galaxy virial mass, M_{200}, at $z = 3.94$ (left-hand panels) and 2.44 (right-hand panels). In the upper panels, the galaxies in filaments and field are shown with red and blue colours, respectively. The solid lines show the median baryonic fractions, while the error bars show the 16th and 84th percentiles of the baryonic fraction in each mass bin. The horizontal dashed line indicates the cosmic baryonic fraction ($\Omega_b/\Omega_m = 0.156$). In the bottom panels, the black lines show the ratios between the median baryonic fractions in filament and field galaxies in different mass bins, and the error is derived by error propagation after symmetrizing the asymmetric errors plotted in the upper panels; see the main text for details. The dotted horizontal line in the bottom panels marks the ratio of 1. Note that we only plot galaxies with $M_{200} \leq 10^{9.5}\ h^{-1}\ M_\odot$, as there are very few field galaxies with masses $M_{200} \gtrsim 10^{9.5}\ h^{-1}\ M_\odot$ in the Auriga simulations.

a higher baryonic fraction (see similar discussions in Okamoto et al. 2008). To study the impacts from these splashback haloes on our results, we have excluded all galaxies that are within $3R_{200}$ of more massive galaxies, and found that the median f_{bar}–M_{200} relations for both our filament and field galaxies are marginally affected.

In Fig. 3, we show stellar fractions of both filament and field galaxies as a function of their parent halo masses. Here, the stellar fraction is defined as $f_{star} \equiv M_{star}/M_{200}$, where M_{star} is the stellar mass inside the virial radius of a galaxy. At both $z \approx 4$ and $z \approx 2.5$, compared to LG19, for galaxies with the same virial masses, the stellar fractions in the Auriga simulations tend to be lower (e.g. for galaxies with $M_{200} \sim 10^9\ h^{-1}\ M_\odot$, the Auriga ones have a median stellar fraction of ~ 1.5 per cent, while the ones in LG19 have a median of ~ 15 per cent). This is a result of the supernova feedback processes, i.e. as has been shown in many previous studies, supernova-driven winds with variable wind velocities used in the Auriga simulations are an effective mechanism in simulations to suppress star formation in low-mass galaxies and to reproduce the observed stellar mass fractions and galaxy stellar mass function at the low-mass end (e.g. Okamoto et al. 2010; Puchwein & Springel 2013; Vogelsberger et al. 2013). Interestingly, although the absolute f_{star} values of Auriga dwarf galaxies are lower than those of similar-mass galaxies in LG19, we can still see that at both redshifts, the Auriga dwarf galaxies in filaments tend to have higher stellar masses than their counterparts in the field, and this environmental difference is larger for galaxies with lower halo masses, which is qualitatively similar to LG19.

In general, our results support the conclusions in LG19 that filaments play a role in assisting gas cooling and enhancing star formation. Similar trends have also been seen for galaxies with higher masses (e.g. virial masses $\gtrsim 10^{10}\ h^{-1}\ M_\odot$) in hydrodynamical simulations in cosmological volumes (e.g. Metuki et al. 2015; Xu et al. 2020). For example, Xu et al. (2020) present the cosmic web dependence of baryonic/stellar fractions for galaxies with $M_{200} \geq 10^{10}\ h^{-1}\ M_\odot$ at $z = 0, 1, 3, 6$ using the EAGLE simulations (Schaye et al. 2015). They find that such cosmic web dependence of baryonic fractions increases with redshift up to $z = 3$ at low masses, but the cosmic web dependence of stellar fractions in their simulations only exist at $z = 0$ and 1. Overall, compared to the filament and void galaxies in these cosmological-box simulations, the differences between the filament and field galaxies in this study are more pronounced, possibly due to the fact that the filament environment has a stronger impact on galaxy formation in low-mass haloes.

In observations, some studies suggest that galaxies residing closer to filaments tend to have higher stellar masses (e.g. Alpaslan et al. 2016; Poudel et al. 2017; Lee et al. 2021), which is consistent with the trend in our simulations. However, we should stress that these studies are usually based on galaxies at much lower redshifts (e.g. $z \lesssim 0.2$).

3.2 Star formation rates and galaxy colours

As shown above, since filaments play a role in assisting gas cooling and star formation, we expect that dwarf galaxies residing in filaments may have higher star formation rates and thus bluer colours. To examine this, we plot the star formation rates ($g - r$ colours) of our galaxy sample as a function of halo mass for both filament and field haloes in Fig. 4 (Fig. 5). To avoid unreliable estimations due to poor resolution, we only consider galaxies with at least 20 gas cells (20 star particles) within R_{200} from the parent sample when computing star formation rates ($g - r$ colours). Furthermore, we only show the median for those mass bins that contain at least 20 galaxies. As
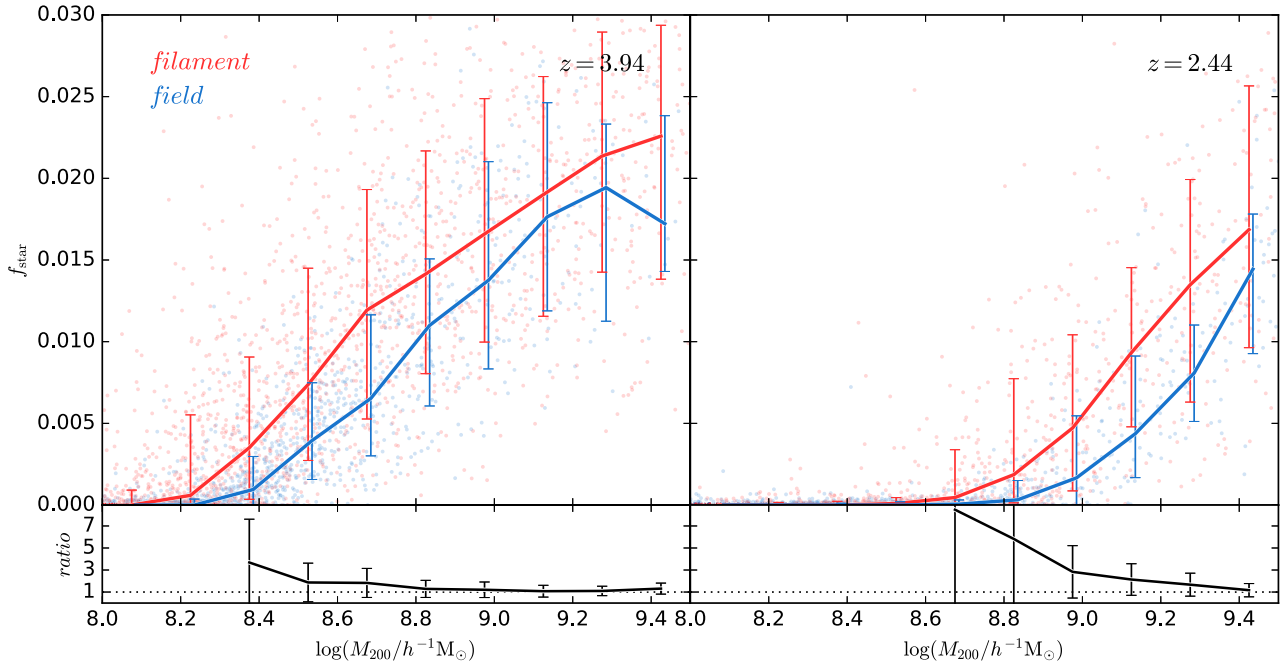
Figure 3. Similar to Fig. 2, but for the stellar fractions, f_{star}.
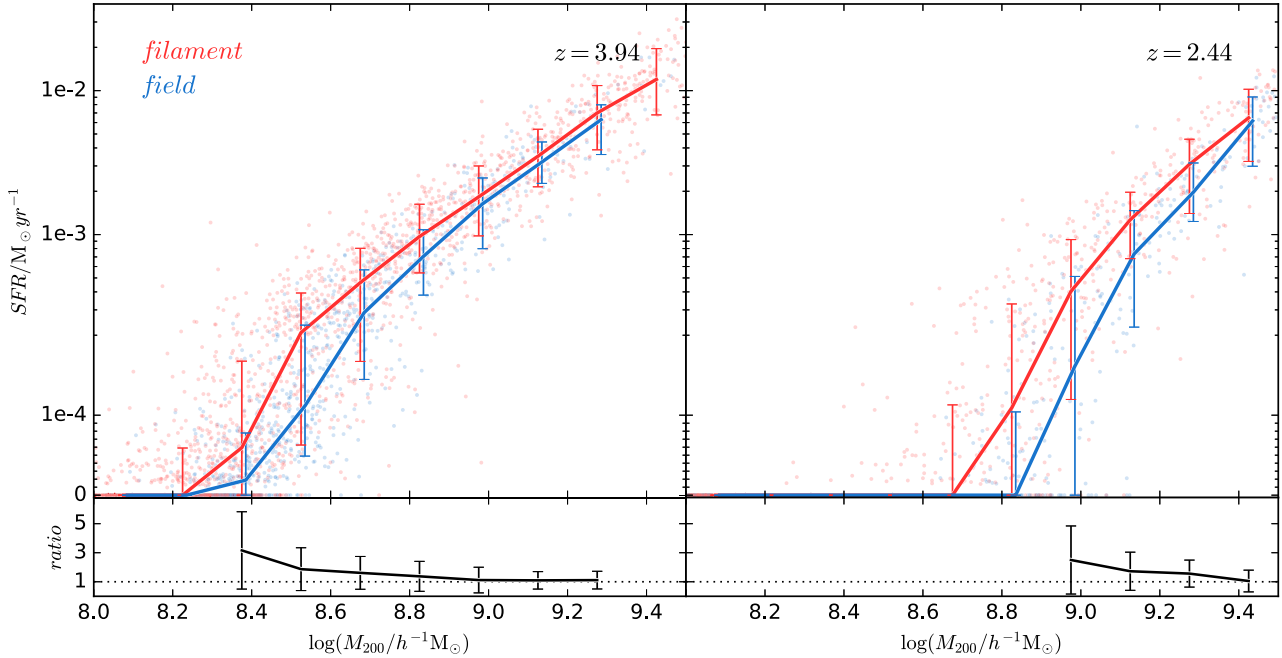

Figure 4. Similar to Fig. 2, but for galaxy star formation rates (SFR). Only galaxies with at least 20 gas cells from the parent sample are considered here. The medians and scatters are only shown for the mass bins containing at least 20 galaxies. Note that in the upper panels, in order to show all the data points, we use a linear scale for $0 \leq SFR \leq 10^{-4} \, M_\odot \, yr^{-1}$ and a logarithmic scale for $SFR > 10^{-4} \, M_\odot \, yr^{-1}$.

expected, dwarf galaxies in filaments tend to have slightly higher star formation rates at both $z \approx 4$ and $z \approx 2.5$ compared to those with similar masses residing in the field. In particular, differences in star formation rates tend to be larger at lower redshifts ($z \sim 2.5$). Our results are consistent with Metuki et al. (2015), who also found that the lowest mass filament galaxies in their sample (i.e. 10^{10}–$10^{11} \, h^{-1} \, M_\odot$) at higher redshifts (i.e. $z \gtrsim 1$) tend to have higher star formation rates than void galaxies. However, apart from the two mass bins of $M_{200} \sim 10^{8.8}$ and $\sim 10^{9} \, M_\odot$ at $z \approx 2.5$ in which the

filament galaxies tend to be slightly bluer, there is no clear difference in galaxy colours between the filament and field populations. In Xu et al. (2020), at $z = 0$, void galaxies in their simulations tend to be slightly redder than filament galaxies with $M_{star} \lesssim 10^{10} \, h^{-1} \, M_\odot$, but such environmental dependence vanishes at $z \geq 1$, which is similar to our results here. On the other hand, our results are inconsistent with some observational results on low-redshift filament galaxies (e.g. Alpaslan et al. 2016; Poudel et al. 2017; Crone Odekon et al. 2018; Lee et al. 2021), which found that galaxies residing closer to
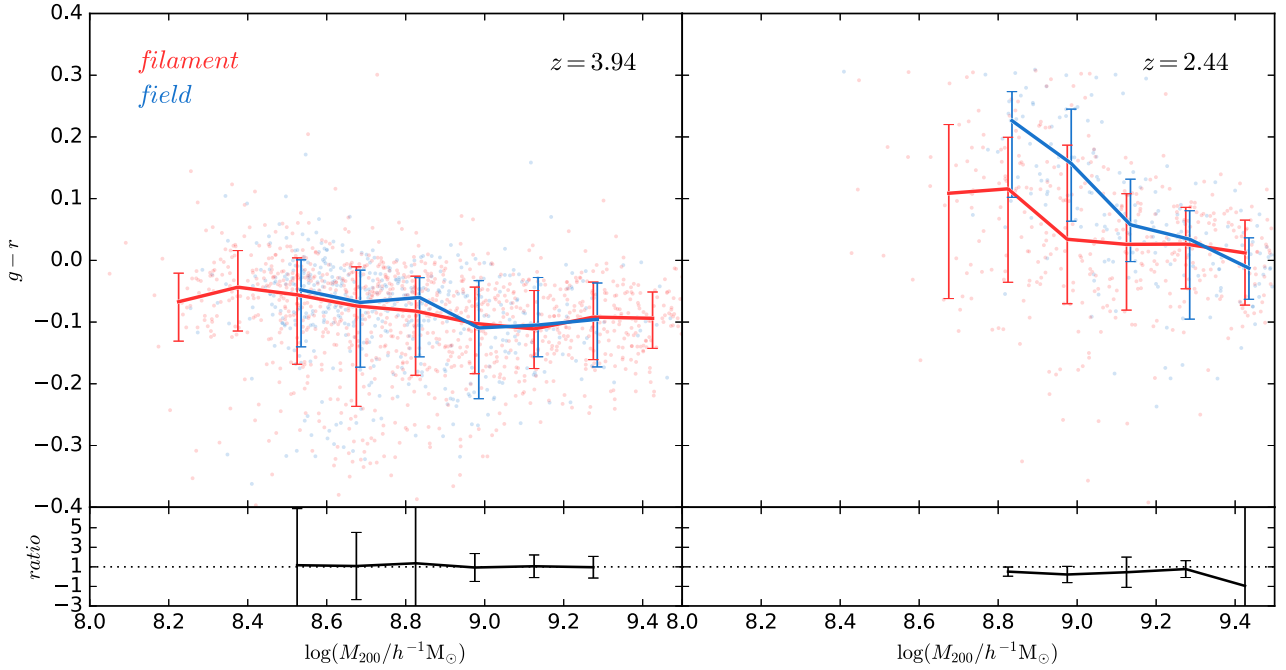
Figure 5. Similar to Fig. 2, but for galaxy colours $g - r$. Only galaxies with at least 20 star particles from the parent sample are used here. The medians and error bars are only shown for the mass bins containing at least 20 galaxies.

filaments tend to be redder and have lower star formation rates. This inconsistency might be due to that properties of the filament galaxies may be different at high and low redshift.

3.3 Alignment between galaxy spins and filaments

As shown in LG19, gas accretion in dwarf haloes in filaments is very anisotropic (i.e. the gas accreting along and perpendicular to the filament forms two distinct modes). It is interesting to study the alignment relation between filaments and their resident dwarfs. In previous studies, the alignment between galaxy orientations and filaments has been investigated with hydrodynamical simulations in cosmological volumes for massive galaxies at low redshift (e.g. Dubois et al. 2014; Codis et al. 2018; Wang et al. 2018; Ganeshaiah Veena et al. 2019; Kraljic, Davé & Pichon 2020). Here, we extend these studies to lower mass dwarf galaxies and to higher redshift with the Auriga simulations.

The alignment between the orientation of a galaxy and the filament in which this galaxy resides can be described as

$$\cos\theta = \frac{\boldsymbol{n}_{\mathrm{spin}} \cdot \boldsymbol{n}_{\mathrm{fila}}}{|\boldsymbol{n}_{\mathrm{spin}}||\boldsymbol{n}_{\mathrm{fila}}|}. \quad (1)$$

Here, $\boldsymbol{n}_{\mathrm{spin}}$ is the spin direction of a galaxy, and $\boldsymbol{n}_{\mathrm{fila}}$ is the direction of the filament in which the galaxy resides. The former one is the same as the direction of the total angular momentum of particles inside R_{200}, and the latter is derived as follows.

Following Hahn et al. (2007), we use the Hessian matrix method to compute filament directions. The Hessian matrix of the smoothed density field at the galaxy centre ($\boldsymbol{x}_{\mathrm{gal}}$) is defined as

$$H_{ij}(\boldsymbol{x}_{\mathrm{gal}}) = \frac{\partial \rho(\boldsymbol{x}; R_{\mathrm{s}})}{\partial x_i \partial x_j}\bigg|_{\boldsymbol{x} = \boldsymbol{x}_{\mathrm{gal}}}, \quad (2)$$

where $i, j = 1, 2, 3$ represent spatial dimensions, $\rho(\boldsymbol{x}; R_{\mathrm{s}})$ is the smoothed filament density field [here, the original filament density field is defined as the baryonic density field composed of the grid cells

that are classified as filament cells; see panels (b) and (e) of Fig. 1], and the smoothing scale, $R_{\mathrm{s}} = 0.25\, h^{-1}\,\mathrm{Mpc}$.[3] Here, the density field is smoothed by convolving with a Gaussian kernel in Fourier space according to Hahn et al. (2007). The filament direction $\boldsymbol{n}_{\mathrm{fila}}$ is then given by the eigenvector that is associated with the maximum eigenvalue of the Hessian matrix. See panels (c) and (f) of Fig. 1 for examples of filament directions (cyan line segments) at the centres of filament galaxies.

In Fig. 6, we plot the alignments ($\langle|\cos\theta|\rangle$) of different components (dark matter, gas, and stellar) of our filament galaxies as a function of their parent halo masses; median values and the 1σ errors are shown. Following previous work (e.g. Ganeshaiah Veena et al. 2019), the 1σ errors are estimated using the bootstrap resampling method. Specifically, in each mass bin, we generate 10^5 realizations with the bootstrap method, compute the median $\langle|\cos\theta|\rangle$ for each realization, and use the standard deviation of all these median $\langle|\cos\theta|\rangle$ as an estimation of the 1σ error. Note that in order to have a numerically robust estimation of the spin direction for the gas component, here we only consider filament galaxies that contain at least 50 gas cells within the virial radius R_{200}. We use a wider mass range [$10^{8.0}$, $10^{10.5}$] $h^{-1}\,\mathrm{M}_{\odot}$ here (as we do not need to consider the mass upper limit of the field sample), and divide it into four mass bins, each of which contains 1108 (542), 614 (367), 278 (239), and 90 (110) galaxies at $z = 3.94$ (2.44). Note that for the stellar component (purple line), we only use galaxies that contain more than 50 star particles [the sample numbers are 251 (218) and 90 (110) at two largest mass bins at $z = 3.94$ ($z = 2.44$)] and only show the results above $10^{9.25}\,h^{-1}\,\mathrm{M}_{\odot}$, which is the approximate value of the corresponding virial mass threshold. It is found that the averaged $|\cos\theta|$ of low-mass dwarf galaxies (especially for the gas component and at $z \sim 2.5$) is larger than 0.5, suggesting that the direction of the spin tends to align with

---

[3]We have tested changing the smoothing scale to 0.1 and $0.5\,h^{-1}$ Mpc, and confirmed that our results are not sensitive to the choice of smoothing scales.
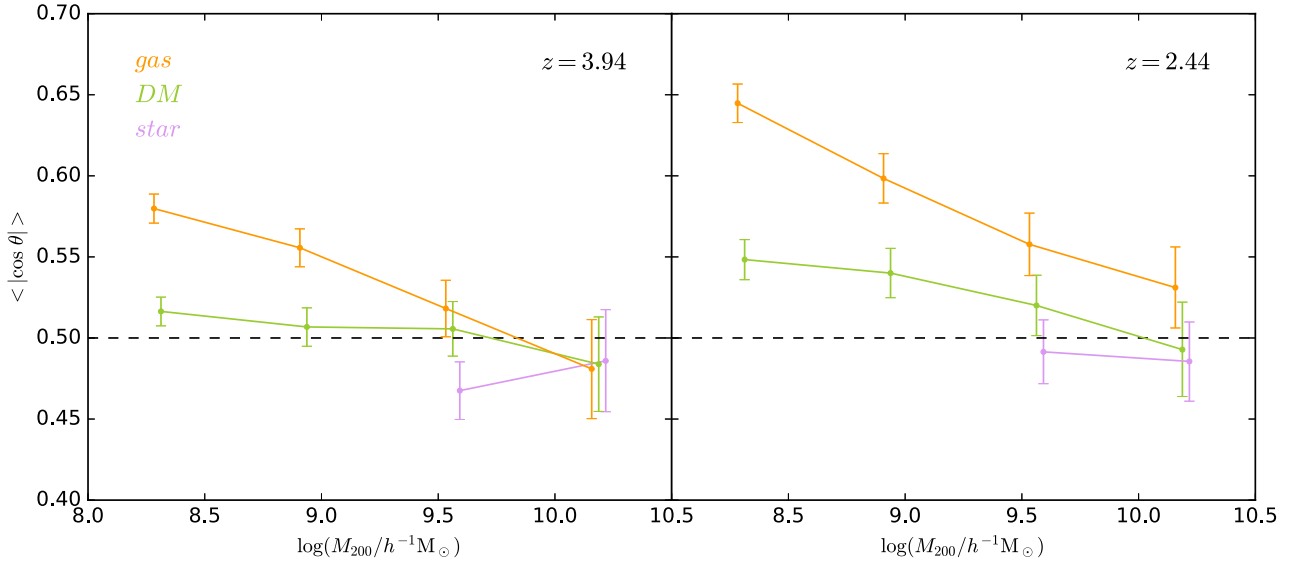
Figure 6. The relation between average $|\cos\theta|$ and galaxy virial mass, M_{200}, at $z = 3.94$ (left-hand panel) and 2.44 (right-hand panel). Orange, green, and purple lines show the results of using gas, dark matter, and star components to compute the spin directions, respectively. The error bars show the 1σ uncertainty estimated by bootstrap resampling; see the main text for details. To be clear, the data points of the dark matter and star components have been slightly shifted along the horizontal axis. The dashed line shows the expected mean value for a uniform $|\cos\theta|$ distribution if no alignments at present.

the direction of the filaments. This trend weakens (even reverses) at larger masses.

This mass dependence of spin–filament alignment in baryonic and dark matter components is broadly in agreement with some previous hydrodynamical simulations (see e.g. Dubois et al. 2014; Codis et al. 2018; Wang et al. 2018; Ganeshaiah Veena et al. 2019; Kraljic et al. 2020), from which it was found that halo/stellar spins of low-mass galaxies tend to be parallel to their filaments, while the halo (or gas) spins of high-mass galaxies tend to be perpendicular to filaments. There is also evidence that this transition mass decreases as redshifts increase (e.g. Wang et al. 2018). But we should note that the spin of the stellar components of our galaxy samples (purple lines in Fig. 6) does not show any clear parallel or perpendicular trend with respect to their filaments, while aforementioned studies (e.g. Wang et al. 2018; Ganeshaiah Veena et al. 2019) suggest a slight perpendicular trend in larger galaxies ($M_{200} \gtrsim 10^{11}\,h^{-1}\,\mathrm{M_\odot}$ or $M_{star} \gtrsim 10^{9}\,h^{-1}\,\mathrm{M_\odot}$). This is possibly due to the fact that we are looking at lower mass and higher redshift galaxies relative to hydrodynamical simulations, and also may be due to the lack of statistics (i.e. we only have two data points in a narrow mass range for stellar components at both redshifts in Fig. 6).

Note that the spin–filament alignment signal for (spiral) galaxies has also been reported in some observations at $z \lesssim 0.2$ (e.g. Tempel & Libeskind 2013; Tempel, Stoica & Saar 2013; Blue Bird et al. 2020; Welker et al. 2020), but these observational results are still quite controversial (see e.g. Zhang et al. 2015; Pahwa et al. 2016; Hirv et al. 2017; Krolewski et al. 2019).

4 CONCLUSION

In this paper, we have made use of the Auriga project, a suite of 30 hydrodynamical zoom-in simulations of Milky Way-like galaxies with a more realistic galaxy formation model, to study the impact of high-redshift dense filaments on their resident dwarf galaxies.

We find that compared to their counterparts in the field, dwarf galaxies residing in filaments tend to have higher baryonic and stellar fractions, and tend to have slightly higher star formation rates at both

$z \sim 4$ and $z \sim 2.5$, in line with LG19, who carried out a similar study with a hydrodynamical simulation with a very simple galaxy formation model without taking into account feedback (though the baryonic and stellar fractions in each environment are generally suppressed by feedback compared to LG19). We also compare the galaxy colours of the filament and field populations, and they do not show a clear difference. Overall, we conclude that dense and massive filaments can enhance the star formation of their resident dwarf galaxies. We also show that the gas components in low-mass filament galaxies at high redshifts tend to have their spins aligned with the filament in which they reside, echoing the spin–filament signal observed for galaxies with higher masses and lower redshifts seen in other hydrodynamical simulations.

DATA AVAILABILITY

The data underlying this paper will be shared on reasonable request to the corresponding author.

REFERENCES

Alpaslan M. et al., 2016, MNRAS, 457, 2287

Audi G., Kondev F. G., Wang M., Huang W. J., Naimi S., 2017, Chin. Phys. C, 41, 030001

Barlow R., 2004, preprint (arXiv:physics/0406120)

Blue Bird J. et al., 2020, MNRAS, 492, 153

Brooks A. M., Governato F., Quinn T., Brook C. B., Wadsley J., 2009, ApJ, 694, 396

Codis S., Jindal A., Chisari N. E., Vibert D., Dubois Y., Pichon C., Devriendt J., 2018, MNRAS, 481, 4753

Crain R. A., Eke V. R., Frenk C. S., Jenkins A., McCarthy I. G., Navarro J. F., Pearce F. R., 2007, MNRAS, 377, 41

Crone Odekon M., Hallenbeck G., Haynes M. P., Koopmann R. A., Phi A., Wolfe P.-F., 2018, ApJ, 852, 142

Davis M., Efstathiou G., Frenk C. S., White S. D. M., 1985, ApJ, 292, 371

Dekel A., Birnboim Y., 2006, MNRAS, 368, 2

Dekel A. et al., 2009, Nature, 457, 451

Dubois Y. et al., 2014, MNRAS, 444, 1453

Ganeshaiah Veena P., Cautun M., Tempel E., van de Weygaert R., Frenk C. S., 2019, MNRAS, 487, 1607

Gao L., Theuns T., 2007, Science, 317, 1527

Gao L., Theuns T., Springel V., 2015, MNRAS, 450, 45

Grand R. J. J. et al., 2017, MNRAS, 467, 179

Hahn O., Porciani C., Carollo C. M., Dekel A., 2007, MNRAS, 375, 489

Hirv A., Pelt J., Saar E., Tago E., Tamm A., Tempel E., Einasto M., 2017, A&A, 599, A31

Hoshen J., Kopelman R., 1976, Phys. Rev. B, 14, 3438

Kereš D., Katz N., Weinberg D. H., Davé R., 2005, MNRAS, 363, 2

Kereš D., Katz N., Fardal M., Davé R., Weinberg D. H., 2009, MNRAS, 395, 160

Kraljic K., Davé R., Pichon C., 2020, MNRAS, 493, 362

Krolewski A., Ho S., Chen Y.-C., Chan P. F., Tenneti A., Bizyaev D., Kraljic K., 2019, ApJ, 876, 52

Lee Y., Kim S., Rey S.-C., Chung J., 2021, ApJ, 906, 68

Liao S., Gao L., 2019, MNRAS, 485, 464(LG19)

Metuki O., Libeskind N. I., Hoffman Y., Crain R. A., Theuns T., 2015, MNRAS, 446, 1458

Ocvirk P., Pichon C., Teyssier R., 2008, MNRAS, 390, 1326

Okamoto T., Gao L., Theuns T., 2008, MNRAS, 390, 920

Okamoto T., Frenk C. S., Jenkins A., Theuns T., 2010, MNRAS, 406, 208

Pahwa I. et al., 2016, MNRAS, 457, 695

Planck Collaboration et al., 2014, A&A, 571, A16

Possolo A., Merkatas C., Bodnar O., 2019, Metrologia, 56, 045009

Poudel A., Heinämäki P., Tempel E., Einasto M., Lietzen H., Nurmi P., 2017, A&A, 597, A86

Puchwein E., Springel V., 2013, MNRAS, 428, 2966

Schaye J. et al., 2015, MNRAS, 446, 521

Springel V., 2010, MNRAS, 401, 791

Springel V., White S. D. M., Tormen G., Kauffmann G., 2001, MNRAS, 328, 726

Springel V. et al., 2008, MNRAS, 391, 1685

Tempel E., Libeskind N. I., 2013, ApJ, 775, L42

Tempel E., Stoica R. S., Saar E., 2013, MNRAS, 428, 1827

Vogelsberger M., Genel S., Sijacki D., Torrey P., Springel V., Hernquist L., 2013, MNRAS, 436, 3031

Wang P., Guo Q., Kang X., Libeskind N. I., 2018, ApJ, 866, 138

Welker C. et al., 2020, MNRAS, 491, 2864

White S. D. M., Frenk C. S., 1991, ApJ, 379, 52

White S. D. M., Rees M. J., 1978, MNRAS, 183, 341

Xu W. et al., 2020, MNRAS, 498, 1839

Zhang Y., Yang X., Wang H., Wang L., Luo W., Mo H. J., van den Bosch F. C., 2015, ApJ, 798, 17

APPENDIX A: RESOLUTION STUDIES

We mainly presented the results for 30 Level 4 (L4) Auriga simulations in the main text. The Auriga project has performed six Level 3
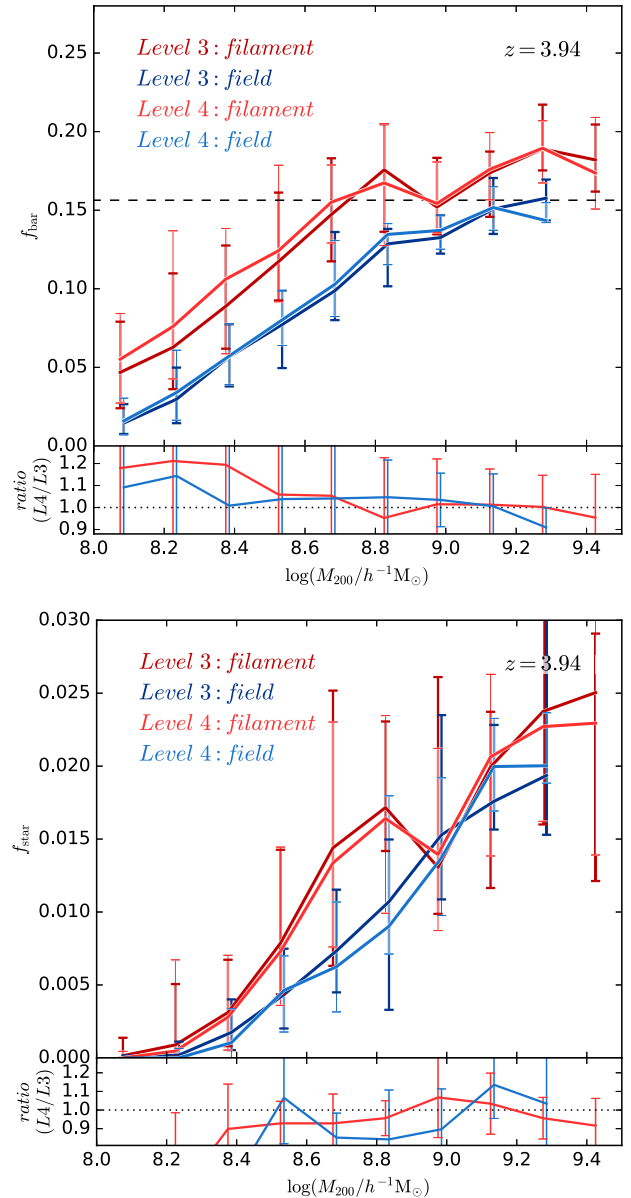

Figure A1. Top panel: resolution convergence of f_{bar}–M_{200} relations. In the upper subpanel, the solid lines show the median relations at $z = 3.94$ for filament (red) and field (blue) galaxies identified from L4 (light colour) and L3 (dark colour) simulations, and the error bars show the 16th and 84th percentiles in each mass bin. The lower subpanel shows the ratio between the L4 and L3 median relations, and the errors of ratios are computed in the same way as those in Fig. 2. Bottom panel: similar to the top panel, but for the resolution convergence of f_{star}–M_{200} relations.

(L3) simulations (i.e. Au-6, Au-16, Au-21, Au-23, Au-24, and Au-27), which have higher resolution (i.e. $m_{DM} = 4 \times 10^4$ M$_\odot$ and $m_b = 6 \times 10^3$ M$_\odot$). To see whether our results in the main text depend on numerical resolution, we have also analysed these six L3 simulations and compared their results with those from the corresponding six L4 simulations.

In the top panel of Fig. A1, we compare the median baryonic fraction–virial mass relations at $z \sim 4$ for both filament and field galaxies from the L4 and L3 simulations. We can see that the relations from the L4 simulations agree fairly well with those from the L3 simulations, i.e. the differences are $\lesssim 20$ per cent in all mass bins.

Especially, the difference in f_{bar} between filament and field galaxies in each mass bin is quite robust in simulations with different resolution, suggesting that our main conclusions are not sensitive to numerical resolution. Similar convergence results can be found for other median relations at both $z \sim 4$ and ~ 2.5 (e.g. the stellar fraction–virial mass relation at $z \sim 4$ shown in the bottom panel of Fig. A1 and other relations that are not shown here).

This paper has been typeset from a TeX/LaTeX file prepared by the author.